JGR Earth Surface

RESEARCH ARTICLE
10.1029/2023JF007298

Beach and Dune Subsurface Hydrodynamics and Their Influence on the Formation of Dune Scarps

Hailey Bond[1], Meagan Wengrove[1], Jack Puleo[2], Maro Pontiki[2], T. Matthew Evans[1], and Rusty A. Feagin[3]

[1]Department of Civil and Construction Engineering, Oregon State University, Corvallis, OR, USA, [2]Department of Civil and Environmental Engineering, University of Delaware, Newark, DE, USA, [3]Department of Ecology and Conservation Biology, Department of Ocean Engineering, Texas A&M University, College Station, TX, USA

Key Points:

- A 1:2.5 scale laboratory experiment was used to study the subsurface hydrodynamics of a beach dune during an erosive event
- Destabilizing pressure gradients were identified within the sand surface, and were impacted by swash conditions and depth within the sand
- A conceptual model for scarp formation is proposed that incorporates observations from this study and could guide future work

Supporting Information:

Supporting Information may be found in the online version of this article.

Correspondence to:

H. Bond,
bondh@oregonstate.edu

Citation:

Bond, H., Wengrove, M., Puleo, J., Pontiki, M., Evans, T. M., & Feagin, R. A. (2023). Beach and dune subsurface hydrodynamics and their influence on the formation of dune scarps. *Journal of Geophysical Research: Earth Surface*, *128*, e2023JF007298. https://doi.org/10.1029/2023JF007298

Received 14 JUN 2023
Accepted 15 NOV 2023

Author Contributions:

Conceptualization: Meagan Wengrove, Jack Puleo, Rusty A. Feagin
Data curation: Hailey Bond
Formal analysis: Hailey Bond, Meagan Wengrove
Funding acquisition: Meagan Wengrove, Jack Puleo, Rusty A. Feagin
Investigation: Hailey Bond, Meagan Wengrove, Jack Puleo, Rusty A. Feagin
Project Administration: Meagan Wengrove, Jack Puleo, Rusty A. Feagin
Resources: Meagan Wengrove
Supervision: Meagan Wengrove
Writing – original draft: Hailey Bond

Abstract Erosive beach scarps influence beach vulnerability, yet their formation remains challenging to predict. In this study, a 1:2.5 scale laboratory experiment was used to study the subsurface hydrodynamics of a beach dune during an erosive event. Pressure and moisture sensors buried within the dune were used both to monitor the water table and to examine vertical pressure gradients in the upper 0.3 m of sand as the slope of the upper beach developed into a scarp. Concurrently, a line-scan lidar tracked swash bores and monitored erosion and accretion patterns along a single cross-shore transect throughout the experiment. As wave conditions intensified, a discontinuity in the slope of the dune formed; the discontinuity grew steeper and progressed landward at the same rate as the $R_{2\%}$ runup extent until it was a fully formed scarp with a vertical face. Within the upper 0.15 m of the partially saturated sand, upward pore pressure gradients were detected during backwash, influencing the effective weight of sand and potentially contributing to beachface erosion. The magnitude and frequency of the upward pressure gradients increased with deeper swash depths and with frequency of wave interaction, and decreased with depth into the sand. A simple conceptual model for scarp formation is proposed that incorporates observations of upward-directed pressure gradients from this study while providing a reference for future studies seeking to integrate additional swash zone sediment transport processes that may impact scarp development.

Plain Language Summary Dunes are important protective features of many sandy coasts around the world. Often, when dune erosion occurs, steep faces known as scarps form. Scarps can erode landward quickly, and it is therefore useful to understand when and where they might form. Here, a large-scale laboratory experiment was used to study the processes involved in the erosion of a dune. The water pressure and moisture content within the dune sediments, and the runup extent and changing elevation of the sand were observed simultaneously. During the experiment, a scarp developed as the wave heights, periods, and water levels increased. As waves passed over the sand surface, the water pressure within the sand changed rapidly, sometimes causing differences (gradients) in pressure between sand at different depths. If the pressure gradients became high enough and were directed upwards, they put an upward force on the sand grains, potentially making them prone to erosion. Upward-directed pressure gradients were observed as wave conditions grew more energetic. To show how the processes observed in this study may have contributed to the formation of the scarp in the experiment, a conceptual model of scarp formation is proposed.

1. Introduction

Dunes are important protective features of many sandy coasts around the world. During storms, dunes are vulnerable to wave collision, overtopping, and subsequent erosion under elevated water levels and wave heights (Sallenger, 2000). When beaches are in an erosive state, near-vertical faces in the foreshore beach profile, called scarps, are a common occurrence (Erikson et al., 2007; Nishi et al., 1995; Sargent & Birkemeier, 1985; Sherman & Nordstrom, 1985; van Bemmelen et al., 2020). After the formation of a scarp, slumping and erosion can occur rapidly, drastically impacting the beach profile (Bonte & Levoy, 2015; Guisado-Pintado & Jackson, 2019). Scarp formation indicates a shift in erosion mechanism. Therefore, the time and location of scarp formation are important elements for the prediction of beach morphological change during erosive conditions. However, the hydrodynamic drivers that cause scarp formation are uncertain, causing predictive models such as XBeach (Roelvink et al., 2010) to estimate scarp development and progression based solely on empirical beach slope thresholds.

Writing – review & editing: Hailey Bond, Meagan Wengrove, Jack Puleo, T. Matthew Evans, Rusty A. Feagin

Physical observations of beach and dune scarps have been used to study their causes. Scarps have been observed to form due to changes in hydrodynamic conditions, also known as process controls (Erikson et al., 2007; Sherman & Nordstrom, 1985; van Bemmelen et al., 2020), or due to the beaches' physical setting, also known as structural controls (Davidson et al., 2020; Sherman & Nordstrom, 1985). Examples of process controls include an increase in wave energy, a change in the angle of wave approach (van Bemmelen et al., 2020), or elevated water levels (Sherman & Nordstrom, 1985). Examples of structural controls include beach nourishments (van Bemmelen et al., 2020), frozen beaches, vehicle tracks (Sherman & Nordstrom, 1985), or vegetation (Feagin et al., 2023). Structural controls like the transition from beach to foredune in the beach profile may also cause scarp formation when exposed to energetic wave conditions. Scarp occurrence at the base of foredunes is common, and its main drivers include mean water level, beach width, and dune slope (Davidson et al., 2020). Combinations of these process and structural controls can lead to a concentration of wave energy on the beachface and the subsequent development of a scarp through shallow slope failures in the swash zone (Bonte & Levoy, 2015; Nishi et al., 1995; Seymour et al., 2005; van Bemmelen et al., 2020).

When some combination of structural and process controls conducive to scarp formation occur, the beach profile gradually steepens, eventually leading to slumping and the formation of a vertical scarp face (Palmsten & Holman, 2011, 2012; van Bemmelen et al., 2020). After the formation of a vertical scarp, the scarp enters the migration phase, in which it moves landward and generally becomes taller. During scarp migration, the mechanism for erosion is slumping and/or undercutting (Leatherman, 1979; Palmsten & Holman, 2011; Sherman & Nordstrom, 1985; Thornton et al., 2007; van Bemmelen et al., 2020). Undercutting of a scarp occurs when the toe of the scarp is eroded in a process known as notching, leaving an unstable mass of sand above the notch (Erikson et al., 2007; Nishi et al., 1995). The mass of sand then develops tension cracks and slumps. Slumping of the beach face can be caused by the infiltration of water into the face of the scarp due to combined high water level and wave impact; the added water increases the sand mass, causes a loss of soil strength, and initiates a failure (Palmsten & Holman, 2011; Sallenger, 2000; van de Graaff, 1994). While Palmsten and Holman (2011) noted that their model did not consider the potential of infiltration to reduce the cohesive force in, and therefore destabilize, the sediment at the base of their modeled scarp, their results suggest that their model of infiltration into the face of the scarp captures the majority of the physics.

Although the process and structural controls of scarp formation have been studied, the direct physical causes of scarp formation have not, to our knowledge, been observed. Therefore, we provide a brief review of previous research on swash zone sediment transport and groundwater dynamics in the swash zone, as those processes could be relevant to erosive and accretive patterns of sand in the swash zone, which could in turn lead to erosion and scarp formation.

1.1. Swash Dynamics, Effective Weight, and Bed Fluidization

Through-bed flow caused by swash typically impacts fine-grained beaches in two major ways: the alteration of effective weight (Baldock et al., 2001; Butt et al., 2001; Hoque & Asano, 2007; Nielsen, 1992; Turner & Masselink, 1998), and the alteration of the boundary layer (Butt et al., 2001; Conley & Inman, 1994). During uprush, a pressure wave propagates into the beachface, leading to elevated pore pressure within the sand. During the subsequent backwash, the pressure at the sand surface is reduced suddenly, and the pore pressure within the beachface exerts an upward-directed force on the sand grains, reducing the effective weight and potentially enhancing offshore transport (Butt et al., 2001; Hoque & Asano, 2007). Alterations of the velocity profile in the boundary layer have the opposite effect. Boundary layer thinning occurs during infiltration (uprush) and causes the streamlines to move closer to the bed, increasing shear stress, while boundary layer thickening occurs with exfiltration (backwash) and causes the streamlines to move away from the bed, reducing shear stress. Therefore, increased onshore sediment transport can be caused by uprush (Turner & Masselink, 1998). Empirical evidence shows that sandy beaches with a grain size less than 0.3 mm are more sensitive to the effect of effective weight alteration than altered boundary layers (Bujan et al., 2019; Butt et al., 2001; Nielsen, 2001). Additionally, while many studies have observed the reduction of effective weight due to upward-directed pressure gradients during backwash (Michallet et al., 2009; Mory et al., 2007; Stark et al., 2022; Tonkin et al., 2003; Yeh & Mason, 2014), several studies have also observed a similar reduction of effective weight under wave crests after a rapid reduction in pressure (Florence et al., 2022; Pujara et al., 2015).

If the pressure gradient caused by backwash is large enough and the effective weight of the particles is reduced to zero, bed fluidization, also known as momentary liquefaction, can occur (Sumer & Fredsøe, 2002). Liquefaction is defined to occur when the effective stress within a sediment matrix equals zero (Holtz & Kovacs, 1981;

Terzaghi, 1943). Momentary liquefaction can occur within coastal sediments under forcing like tsunamis (Yeh & Mason, 2014) and waves (Florence et al., 2022; Michallet et al., 2009; Mory et al., 2007). In coastal applications, momentary liquefaction is often studied by examining the flow velocity (Turner & Nielsen, 1997) or by examining pressure gradients (Florence et al., 2022; Michallet et al., 2009; Mory et al., 2007; Stark et al., 2022; Tonkin et al., 2003; Turner & Masselink, 1998; Yeh & Mason, 2014). Different studies propose various thresholds for momentary liquefaction.

Turner and Nielsen (1997) explain that in the swash zone, vertical flow occurs in the direction of decreasing flow potential. Using Darcy's law, they give the critical velocity for bed fluidization as:

$$w_{crit} = K(\rho_b/\rho - 1), \tag{1}$$

where w_{crit} is the critical vertical flow velocity that causes bed fluidization, K is the hydraulic conductivity of the bed, ρ_b is the bulk density of the bed, and ρ is the fluid density.

Rather than use fluid velocity to determine criteria for liquefaction, Mory et al. (2007) and Michallet et al. (2009) use a pressure difference (converted to an equivalent water depth), and account for the gas content within the sediment to empirically determine the threshold for liquefaction. Momentary liquefaction is sensitive to gas content within the sediment (Gratiot & Mory, 2000; Michallet et al., 2009; Mory et al., 2007; Okusa, 1985; Sakai et al., 1992) because gas can dampen pressure waves and alter the phase shift that occurs as the pressure wave propagates into the sand. Gas content is difficult to measure, but has been observed at magnitudes of at least a few percent in fully submerged sediments in the field (Mory et al., 2007). Mory et al. (2007) and Michallet et al. (2009) use the following equation:

$$\Delta P > \rho g h\left[\rho_s/\rho(1-\epsilon) + \epsilon - \epsilon C_{gas}(1-\rho_*/\rho)\right], \tag{2}$$

where ΔP is the threshold pressure difference between the pressure at two known locations required to cause momentary liquefaction, h is the distance between locations of interest, ρ_s and ρ_g are the densities of sediment and gas, respectively, ϵ is the porosity of the soil, and C_{gas} is the gas content. In the equation of Mory et al. (2007), $\rho_* = \rho_g$, and in the equation of Michallet et al. (2009), $\rho_* = \rho_s$.

The definition of momentary liquefaction can also be used to determine whether liquefaction is occurring. Momentary liquefaction is defined mathematically as follows (adapted from Sumer and Fredsøe (2002)):

$$dh_d/dz > (\gamma_{sat} - \gamma)/\gamma, \tag{3}$$

where h_d is the dynamic pore pressure converted to meters of water, γ_{sat} is the saturated density of the soil, and γ is the fluid density.

The modification of effective weight caused by backwash disrupts the equilibrium of forces acting on the sand grains, irrespective of whether the conditions for momentary liquefaction are met. The destabilization of sediments has the potential to intensify erosion, as observed in previous studies (Butt et al., 2001). The contribution of effective weight to sediment transport is demonstrated in the altered Shields parameter proposed by Turner and Masselink (1998), and has been shown to be related to erosion in Tonkin et al. (2003). In this work, the terms "upward-directed pressure gradient," "destabilizing event," or "destabilization" are used to refer to instances when dh_d/dz is negative, potentially reducing the effective weight of the sand, and the term "momentary liquefaction" is used to refer to times at which one or more of the liquefaction thresholds (Equations 1–3) is met.

1.2. Groundwater Hydrodynamics

Beach groundwater can impact the erosion and accretion of sediments on a beach profile. Typically, beach groundwater near the swash zone has a saturated area which is elevated above the still water level (SWL) because of wave action (Gourlay, 1992; Raubenheimer et al., 1999; Turner & Nielsen, 1997). The elevation of the groundwater above the SWL depends on sediment permeability, beach morphology, wave and surge conditions, and tidal phase (Paldor et al., 2022; Turner & Nielsen, 1997). The shape of this super-elevation is skewed with time, meaning that the water table raises faster than it lowers (Emery & Foster, 1948; Turner & Nielsen, 1997). A capillary fringe, in which pore pressures are negative, exists above the groundwater table (Figure 5). The height of the capillary fringe depends on the sediment grain size (Turner & Nielsen, 1997). The groundwater table intersects the beachface at the exit point, below which water seeps out of the beach at the seepage face. The groundwater level is not static, and in the field, changes with the tides and wave conditions (Bakhtyar et al., 2011; Eliot & Clarke, 1988;

Heiss et al., 2015; Paldor et al., 2022). On a rising tide, the groundwater level lags behind the tide level by 2–3 hr, which can cause accretion near the swash limit and erosion in the swash zone (Duncan, 1964). When groundwater is rising, it can trap air bubbles, leading to a high gas content within the pore spaces (Michallet et al., 2009; Mory et al., 2007). Groundwater conditions also have the potential to decrease the stability of the beach during storm surge events (Paldor et al., 2022).

Process and structural controls (e.g., changes in wave energy and the shape of the beach profile) have been associated with scarp formation through several field studies (Bonte & Levoy, 2015; Nishi et al., 1995; van Bemmelen et al., 2020). In the lab and in the field, the landward erosion of a scarp after its formation has been studied in detail (Bonte & Levoy, 2015; Palmsten & Holman, 2011; van Bemmelen et al., 2020). However, swash zone sediment transport processes occurring during scarp formation have yet to be investigated. Scarps form most often in erosive conditions that make field measurements of surface and subsurface processes difficult, if not impossible. The objective of this study is to use a laboratory experiment to quantify the time and location of scarp formation during an erosive event, and to identify physical processes that contribute to its development. We present data from a 1:2.5 scale laboratory experiment involving the erosion of a dune and the formation of a scarp under scaled extreme conditions, including data collected from moisture sensors, pressure sensors, and a line-scan lidar.

2. Methods

2.1. Experimental Setup

Collecting data in the field during significant dune erosion events is technically challenging and therefore, data of subsurface hydrodynamics during dune scarping are limited. For this reason, a laboratory experiment was designed to enable the collection of detailed, high frequency measurements of the subaerial and subsurface processes that contribute to dune erosion. The experiment took place in the NSF NHERI O.H. Hinsdale Wave Laboratory Large Wave Flume (LWF) at Oregon State University. The LWF channel is 104 m long, 3.7 m wide, and 4.6 m tall. The piston-style wavemaker can generate waves up to 1.7 m at a maximum water depth of 2.7 m. The wavemaker is equipped with active wave absorption, but this functionality was turned off at significant wave heights above 0.90 m due to mechanical limitations of the wavemaker.

A dune profile was constructed within the flume using sand removed from the South Beach jetty in Newport, Oregon and compacted with a vibrating plate compactor in 0.3 m lifts to achieve a compaction near that of a natural dune. The similarity in compaction of the scaled dune in the lab and a natural dune sampled in the field was confirmed with dynamic cone penetrometer testing (Figure 3 in Supporting Information S1). The sand was poorly graded with a d_{50} of 0.21 mm, and had minimum and maximum possible void ratios of 0.61 and 0.77, respectively. The initial dune profile was selected for the presence of its berm seaward of the main dune and its ideal dimensions when scaled to the size of the flume, and was based on a 2012 survey of a dune in Mantoloking, New Jersey. The d_{50} of the sand in Mantoloking is 0.39 mm, so both the dune dimensions and sediment size were considered in the scaling process.

The experimental wave conditions were scaled from observed conditions during Hurricane Sandy in 2012 (Pontiki et al., 2023). The water levels were based on data observed at the Atlantic City NOAA Tides and Currents Station (NOAA, 2023), and the significant wave heights and wave periods throughout the duration of the storm were based on the random phase spectral model WAVEWATCH III offshore of Mantoloking (WW3DG, 2019). Forcing conditions and dune geometry were scaled using a two free parameter scaling method developed specifically for beach and dune erosion processes (Van Rijn et al., 2011). The two free parameters used were the sediment size scale ($n_{d50} = 1.89$) and the depth scale ($n_h = 2.5$), yielding the length scale ($n_l = 2.49$) and the time scale ($n_T = 1.58$). The scaled water depth, wave height, and wave period data were fit with exponential curves and discretized into 47 individual wave trials (Figure 1). The wave parameters were converted to time series using a TMA spectrum. Each trial contained 300 waves, and trials ranged between 16 and 36 min depending on the wave period (Figure 1). Wave energy was allowed to settle between trials for between 1 and 2 hr.

2.2. Instrumentation

The interior of the dune was instrumented (Figure 2) with 15 Druck PCDR 1830 pressure sensors and 30 Teros-10 moisture sensors during construction. The pressure sensors were vented and measured gage pressure, while the moisture sensors measured volumetric water content. The sensors sampled at 100 Hz and were used to evaluate the effects of individual waves on the dune surficial sediments near the expected location of scarp formation and the porewater hydrodynamics deeper in the dune. The sensor naming convention is: the first letter refers to the

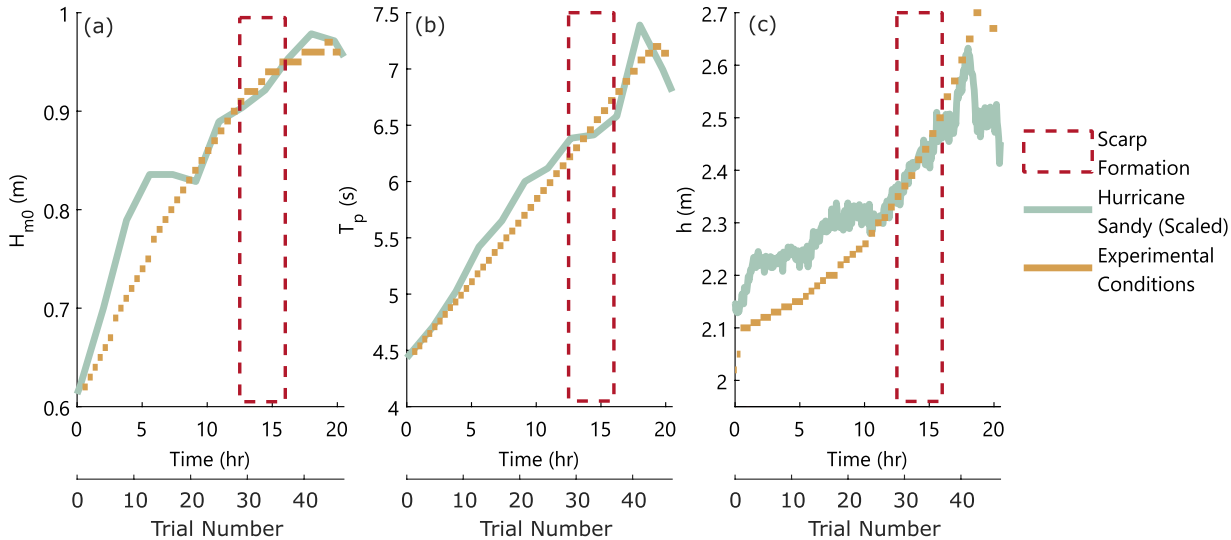

Figure 1. Forcing conditions for laboratory experiment (orange) compared with modeled data of storm event (turquoise). (a) Spectral significant wave heights, (b) wave periods, and (c) water levels. Red dashed regions show the time period of scarp formation (Trials 34–41). The upper *x*-axis reflects the actual duration of wave forcing in the lab, the lower *x*-axis reflects the associated trial numbers.

sensor type ("M" for moisture sensors and "P" for pressure sensors), the second two numbers refer to the cross shore location of the sensor ("77" means the sensor was located at $x = 77$ m), and the last letter refers to how deep the sensor was buried ("a" is the shallowest sensor).

To measure runup and track the erosion of the dune throughout the experiment, a Reigl Z390i line-scan lidar (6 mm accuracy, 0.001° vertical angle resolution) was set up on an instrument cart above the flume to provide a view of the dune and berm. Throughout the wave trials, the lidar continuously scanned a single cross-shore transect at approximately 2 Hz, capturing the water surface elevation, runup elevations, and changes in the dune profile.

2.3. Signal Processing

2.3.1. Pressure Sensors

The measurements from the pressure sensors were analyzed to assess the pressure fluctuations within the dune due to waves. Additionally, the sensor data was used to track the water level within the dune. The raw measurements

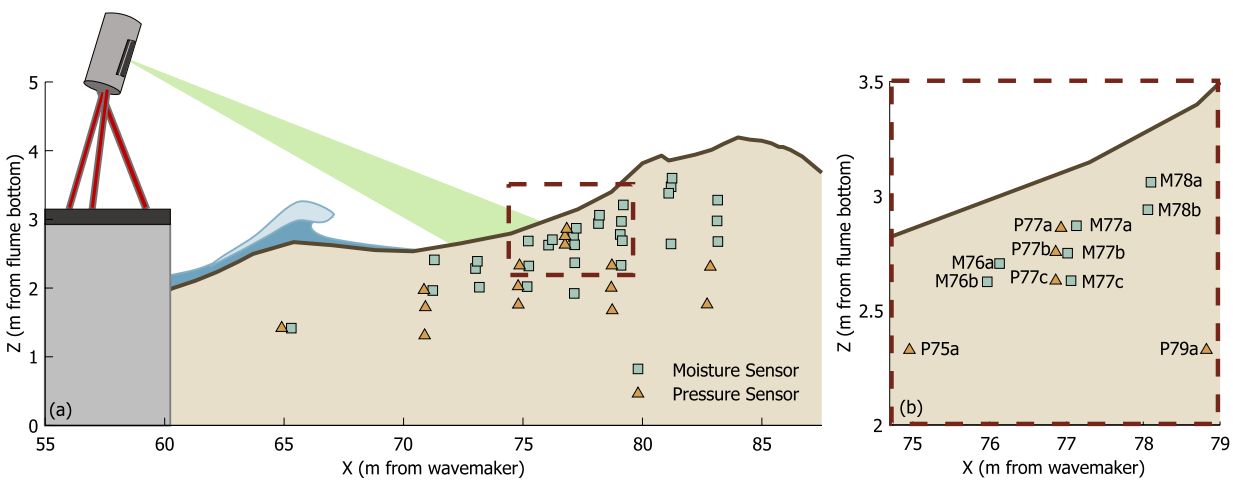

Figure 2. (a) Locations of moisture and pressure sensors within the dune and the lidar location and view for monitoring runup elevations and dune morphology. (b) A close-up view of the sensors used for analysis in this study.

were initially calibrated using calibration coefficients provided by the sensor manufacturer. However, during the 5 month interval between instrument installation and experiment, the pressure sensor measurements exhibited drift. To address the sensor drift, the dune water table was assumed still, constant, and at the same elevation as the water level in the flume during a period of time when the waves were not being generated. By comparing the expected pressure sensor outputs based on the flume water level with the actual sensor outputs, the drift for all measurement periods was calculated and removed. These adjustments were carried out before Trial 27, when the water table was expected to reach $z = 2.26$ m, placing pressure sensors P75a, P77c, and P79a (Figure 2) in the range of the 0.3–0.4 m capillary rise predicted by Turner and Nielsen (1997). However, the pre-adjustment pressure measurements for all sensors considered in this analysis were positive, and the upper sensors used for further calculations all had adjustments of less than 0.01 m of pressure head.

To isolate the fluctuations in excess pore pressure due to waves, porewater pressure measurements from sensors P75a, P77a-c, and P79a (Figure 2b) were filtered with a 30 s moving minimum filter. The filtered time series was then smoothed with a 50 s moving mean filter. This processed time series shows the rising water table throughout the progression of each trial (Figure 1a in Supporting Information S1), and is referred to hereafter as static pressure. Subsequently, the static pressure was subtracted from the total pressure signal to separately examine the effect of waves on the pressure signal (Figure 1b in Supporting Information S1). This time series is referred to hereafter as the dynamic pressure. To calculate the apparent elevation of the water table within the dune (i.e., the water table if hydrostatic pressure was assumed), the static pressure was converted to an equivalent depth and added to the elevation of the sensor. To visualize the apparent water table in the area of scarp formation, the apparent water table was interpolated between sensors P75a, P77c, and P79a.

Pressure gradients and the potential for momentary liquefaction were calculated using the dynamic pressure time series (after Sumer and Fredsøe (2002)):

$$dh_d/dz = (p_{d,upper} - p_{d,lower})/\gamma(z_{upper} - z_{lower}), \quad (4)$$

where dh_d/dz is the dynamic pressure gradient (unitless), $p_{d,upper}$ and $p_{d,lower}$ are the dynamic pressures (in Pa) at the upper and lower sensors, respectively, γ is the unit weight of water (in N/m^3), and z_{upper} and z_{lower} are the elevations, in m, of the upper and lower sensors, respectively. The sign convention used here means that a negative pressure gradient is upward-directed (i.e., the lower sensor has a higher dynamic pressure than the upper sensor) and a positive pressure gradient is downward-directed (i.e., the upper sensor has a higher dynamic pressure than the lower sensor).

2.3.2. Lidar-Derived Beach Change and Runup Statistics

For every trial of the experiment, two lidar scans were taken. The first was a frame scan prior to each trial that captured the subaerial portion of the dune, the flume walls, and three reflectors within the flume. The second was a line scan taken along a single cross-shore transect throughout the duration of the trial that captured the surface elevations of the water and the sand. The frame scans were used to calculate transformation matrices for every trial to transform the data from the lidar's coordinate system to the wave flume coordinate system. These transformation matrices were then used to rectify the line scans for further analysis. The transformation matrices for the frame and line scans were calculated with a plane-matching algorithm (O'Dea et al., 2019). The algorithm found points on 10 planes along the walls of the wave flume and used a least squares fit to match the points to corresponding mathematical planes created from a baseline scan of the wave lab.

The line scans were taken with a 0.001° resolution in both the horizontal and vertical directions at approximately 2 Hz for the duration of each trial. The line scans were used to track profile changes and determine the swash depth. After gridding the scans at a resolution of 0.005 m in the cross-shore, the sand surface was identified using a 25 s moving minimum filter. In the swash zone, where the sand surface was intermittently submerged, the moving minimum at each grid point was interpreted as the sand surface. Using the sand surface elevation, the dune slope was calculated at each grid point with a 0.25 m cross-shore window.

After the sand surface was identified, swash depths were determined by computing the difference between the water/sand surface elevations and the filtered sand surface locations. The runup location at each time step was defined as the farthest cross-shore location where the swash depth was less than 0.02 m. Runup exceedance excursions for the $R_{16\%}$, $R_{10\%}$, and $R_{2\%}$ exceedance probabilities were calculated with cumulative probability distributions based on the runup measurements from each trial. The runup exceedance excursions represent the cross-shore

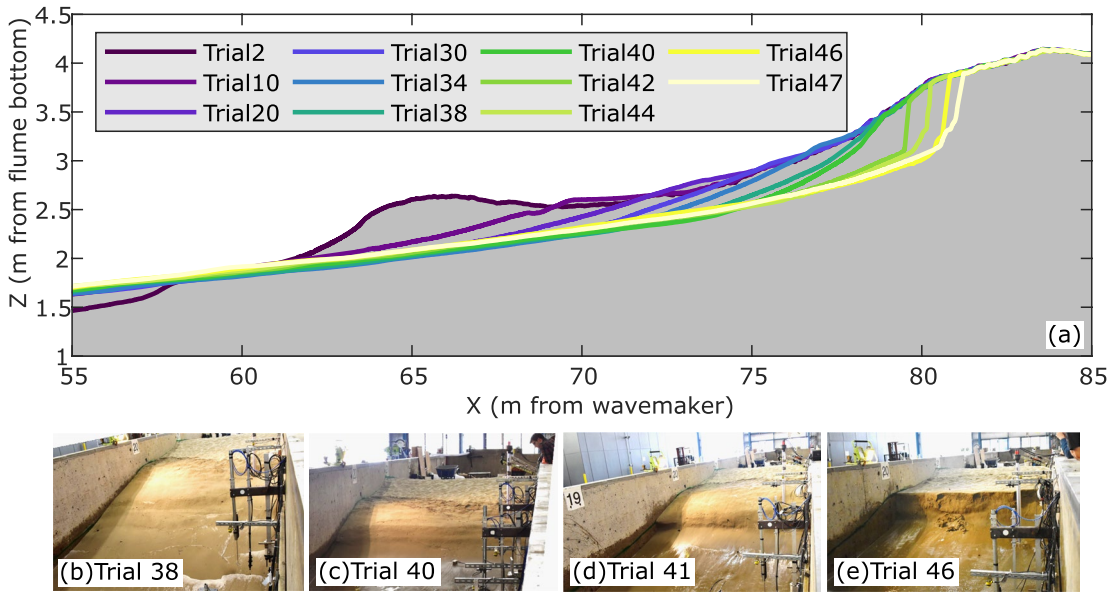

Figure 3. Dune profile evolution (top) and corresponding photos of scarp evolution (bottom). The time intervals between profiles are uneven, as the dune eroded slowly at first and quickly at the end of the experiment.

excursion exceeded by a certain percentage of runup events (Holman, 1986). The maximum cross-shore runup was also found for each trial. To characterize the swash at specific locations, $h_{2\%}$ (calculated as the depth of the highest 2% of swash events during some observed time period) and the swash return period T_{avg} (calculated as the length of some observed time period divided by the number of swash events recorded) were used.

2.3.3. Moisture Sensors

To calibrate the Teros-10 moisture sensors, 15 sensors in groups of 5 were sampled in a dune sand sample at six different water contents. These water contents ranged from air-dried sand (gravimetric water content of approximately 0%) to the highest saturation possible within the calibration setup (gravimetric water content of 20%–30%). At each water content, the sensors were buried in the sand sample several times to calculate an average voltage reading for each water content. A cubic function was fit to the calibration data for each sensor (Figure S2 in Supporting Information S1). Subsequently, voltage records were related to sediment moisture content using the average of the 15 calibration curves. Because the moisture sensors measure volumetric water content, the water content recorded by the sensor is influenced by the void ratio of the sand (i.e., in saturated sands with different void ratios, the volumetric water content of the sediment will be different). Therefore, the fluctuations of single sensors were used for qualitative reference rather than comparing the volumetric water content between sensors.

3. Results

Results focus on observations of subsurface dune hydrodynamics during the formation of a dune scarp, with emphasis on the period of scarp formation between Trials 34 and 41. Results showed the formation of a scarp as the wave conditions became more energetic and water levels increased. Within the dune, the groundwater table rose and sediments in the swash zone became partially saturated. Instances of upward-directed pressure gradients increased in later trials, but very few instances of momentary liquefaction were observed based on the criteria given in Equations 1–3.

3.1. Dune Scarp Morphological Development

The experimental beach profile consisted of a berm seaward of a dune. The berm eroded over the first 11 of 47 total trials (Pontiki et al., 2023) (Figure 3). After the berm eroded and the berm sediments were transported offshore, the remaining beach profile was concave. The beach profile retreated landward from Trials 10–34. By Trial 34, a local maxima in the beach slope (hereafter referred to as the developing scarp) formed in the beach profile at x = 76.5 m (Figure 3). The developing scarp continued to steepen and move landward from Trials 34–41 as the

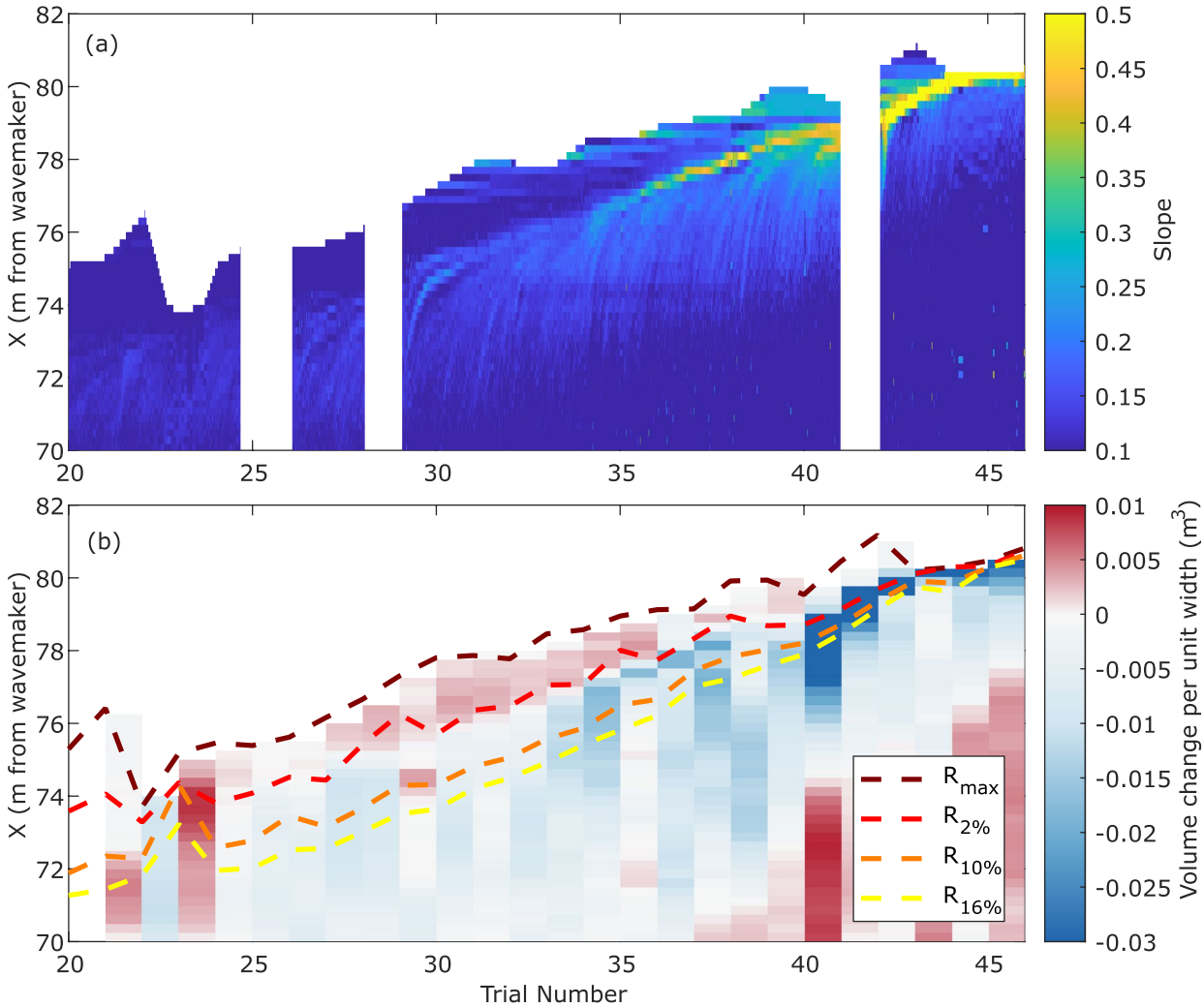

Figure 4. Changes in dune properties between Trial 20–47. (a) Space-time representation of the dune steepness. Green and yellow colors indicate the presence of a developing scarp. (b) Erosion and accretion along the profile during different trials. Note the period of accretion between Trials 28–36 and cross-shore locations $x = 75$–78 m, and the increasing erosion beginning during Trial 34. Runup exceedance extents (the cross-shore distance exceeded by some percentage of runup events) are also included.

lower beach profile continued to erode. The developing scarp formed between the $R_{10\%}$ and $R_{2\%}$ runup exceedance extents and remained between those locations as the waves, water levels, and therefore runup exceedance extents increased (Figure 4). During Trial 42, the steep face began to slump, leading to the presence of a sharp vertical face at $x = 79.5$ m at the end of the trial (Figure 3a). We consider the scarp fully formed at the end of Trial 42 due to its vertical face. The scarp retreated landward to $x = 81$ m throughout the remainder of the trials (Figure 3).

While the profile eroded and moved landward, accretion occurred between the $R_{2\%}$ runup exceedance extent and the $R_{\max}$ location during Trials 28–36 (Figure 4b). The location of the accretionary deposits moved as the water level, wave height, and therefore runup elevation increased throughout the experiment. When the scarp began developing during Trial 34, the profile elevation at the upper slope break was 0.05 m higher than it had been at that location at the start of the experiment (Figure 3b).

3.2. Dune Groundwater Hydrodynamics

As the wave height, wave period, and water level increased, the elevation of the apparent groundwater table also increased. The apparent groundwater table was elevated beneath the swash zone and its elevation varied in the cross-shore. The height of the apparent groundwater table (calculation details given in Section 2.3.1) was driven by a static component caused by the increasing water level in the flume, and a wave driven component. Thus, the

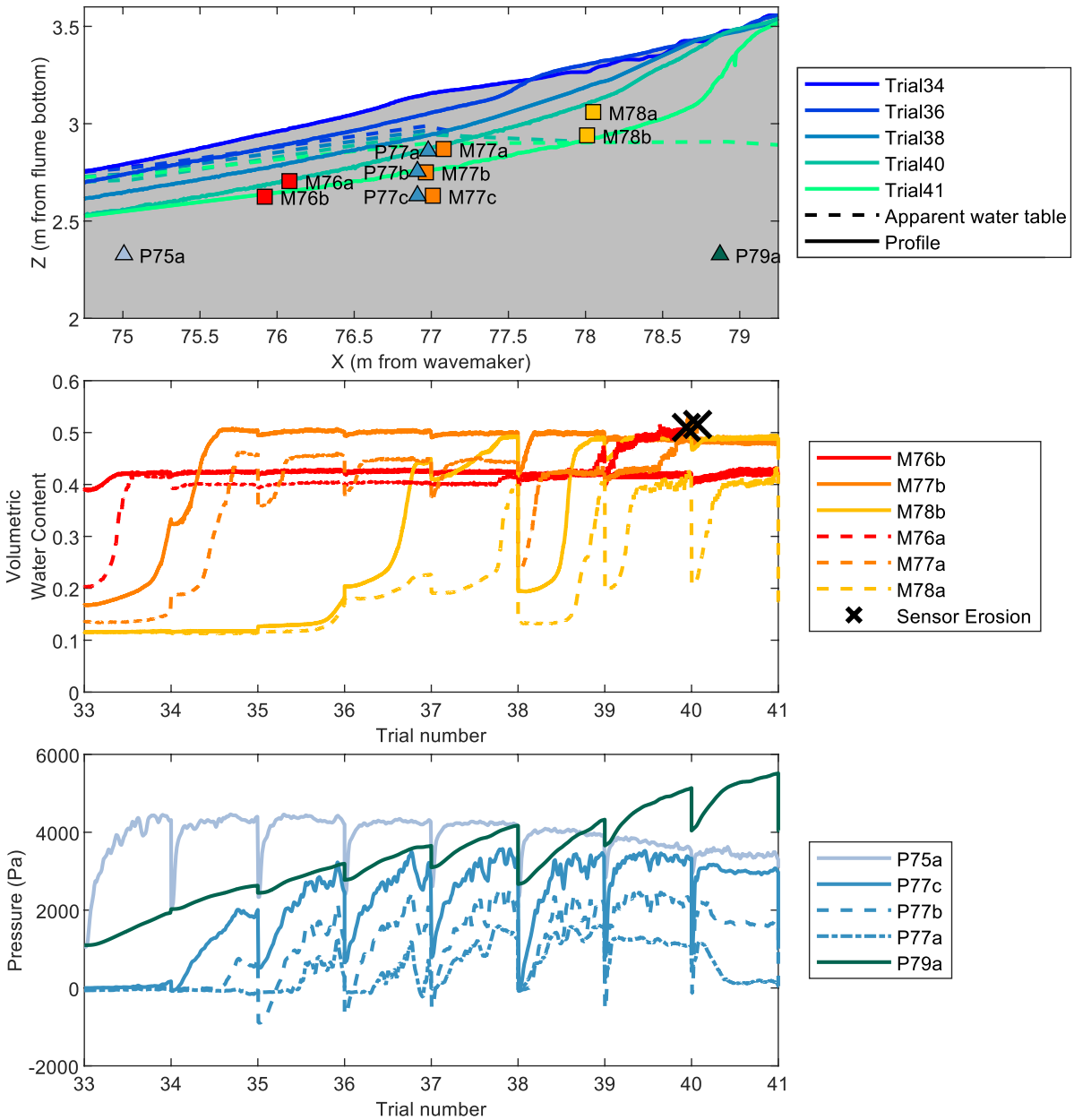

Figure 5. (a) Profile evolution (solid lines) and representation of apparent water table evolution (dashed lines) during scarp formation. The apparent water table height was calculated based on the static pressure recorded at pressure sensors P75a, P77c, and P79a. (b) Evolution of volumetric water content over the course of scarp formation. Different colors represent sensors at different cross-shore locations as displayed in (a). Different line types represent different sensor elevations. (c) Pressure changes during the course of scarp formation. Different colors represent sensors at different cross-shore locations as displayed in (a). Different line types represent different sensor elevations.

apparent groundwater table rose and lowered throughout the experiment as waves were stopped for several hours to complete measurements between trials (Figures 5b and 5c).

The movement of the apparent water table was also visible in the moisture sensor measurements. For moisture sensors between the heights of the apparent static and wave driven water table, the water content increased over the course of each trial, sometimes reaching a steady state of partial saturation (e.g., Trials 34 and 35, sensor M77a, Trial 33, sensor M76a). The steady state was unlikely to be full saturation, given that volumetric gas contents of at least a few percent are regularly observed within fully submerged sands (Michallet et al., 2009; Mory et al., 2007; Okusa, 1985). Moisture contents did not appear to increase after that plateau until the sediment was disturbed by swash (Sensors M76a, M77a, Trial 39).

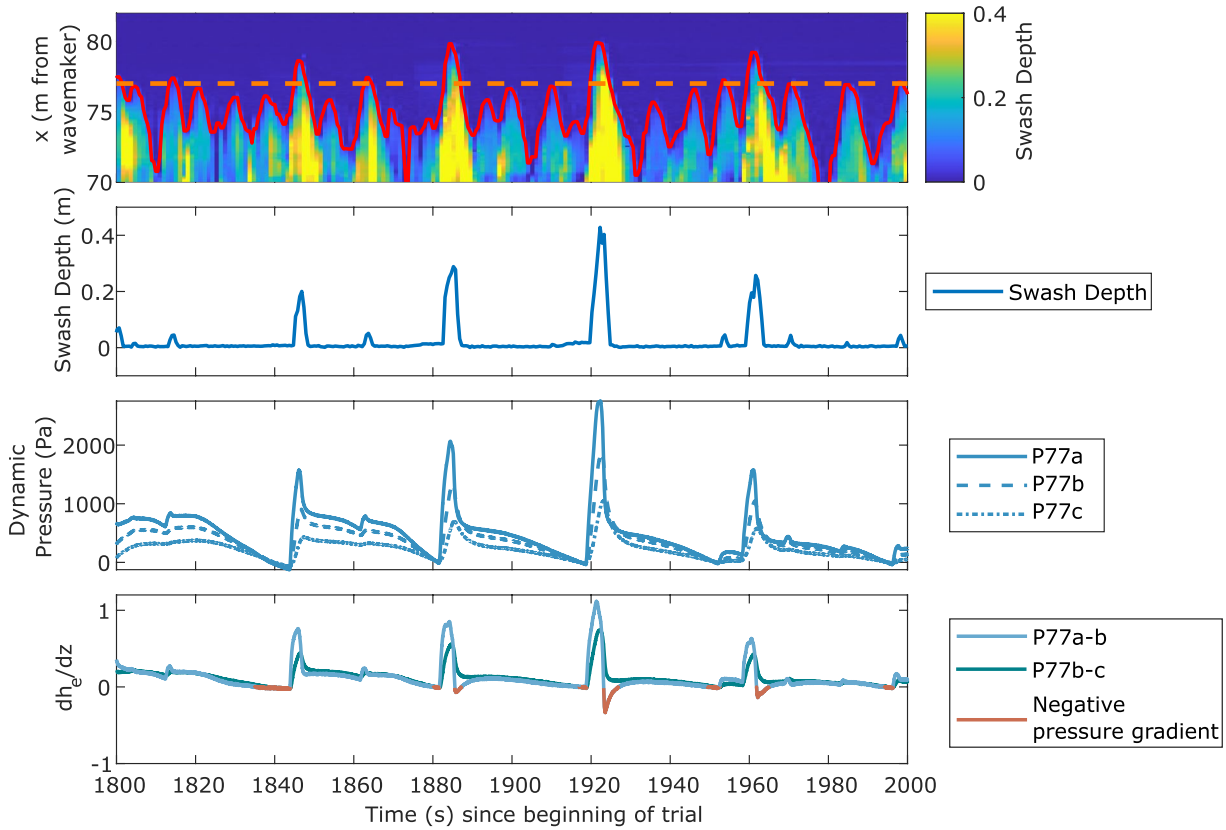

Figure 6. A excerpt of 200 s of data from Trial 38: (a) time stack of swash depth, with runup extent marked in red and the cross-shore location of sensors marked in the orange dashed line, (b) time series of swash depth at location of sensors, (c) dynamic pore pressure for sensors P77a, P77b, and P77c (d) dynamic pore pressure gradients between sensors P77a-b and P77b-c, with negative gradients shaded in red.

Measurements of volumetric moisture content qualitatively agreed with measurements of the apparent groundwater table where moisture and pressure sensors were co-located. Moisture sensor M77a had just reached a steady partial saturation at the end of Trial 34 (Figure 5), which agrees with the measurement of apparent water table at $x = 77$ m at the end of Trial 34 (Figure 5a). At $x = 78$ m, where only moisture sensors are located, moisture sensor M78a is steadily partially saturated beginning in Trial 37 (Figure 5b), which is earlier than predicted by the interpolated apparent water table at $x = 78$ m (Figure 5a).

3.3. Dune Pore Pressure Gradients

During the formation of the scarp in this experiment, negative (upward-directed) vertical gradients in dynamic pore pressure were observed during backwash. When waves ran up the beach, increases in dynamic pressure were observed in the sand. When the waves receded, the dynamic pressures at the surface instantaneously decreased. However, the dynamic pressures lower in the sand had not yet dissipated, causing negative pressure gradients within the sand. As an example, a 200 s period of Trial 38 is shown (Figure 6). During runup events (Figure 6), the dynamic pressure was higher at pressure sensor P77a than pressure sensor P77b, causing a positive (downward-directed) pressure gradient. As the swash-induced dynamic pressure propagated through the sand, the pressure sensor P77b recorded an increase in dynamic pressure as the swash transitioned into its backwash phase. This led to a release of pressure in sensor P77a, resulting in a reversal of the excess pore pressure gradient and the emergence of a negative, upward-directed dynamic pressure gradient (Figure 6d; shaded in red).

Patterns of negative pressure gradients recorded by sensors were influenced by changing wave conditions and the changing sand cover over the sensor during erosion. To isolate the effect of the changing wave conditions, the gradient between sensors P77a and P77b and the gradient between sensors P77b and P77c were compared as the sand cover over the upper sensors eroded from 0.16 to 0.1 m (from 900 to 1,900 s of Trial 38 for sensors P77a and P77b, from 500 to 1,500 s of Trial 40 for sensors P77b and P77c).

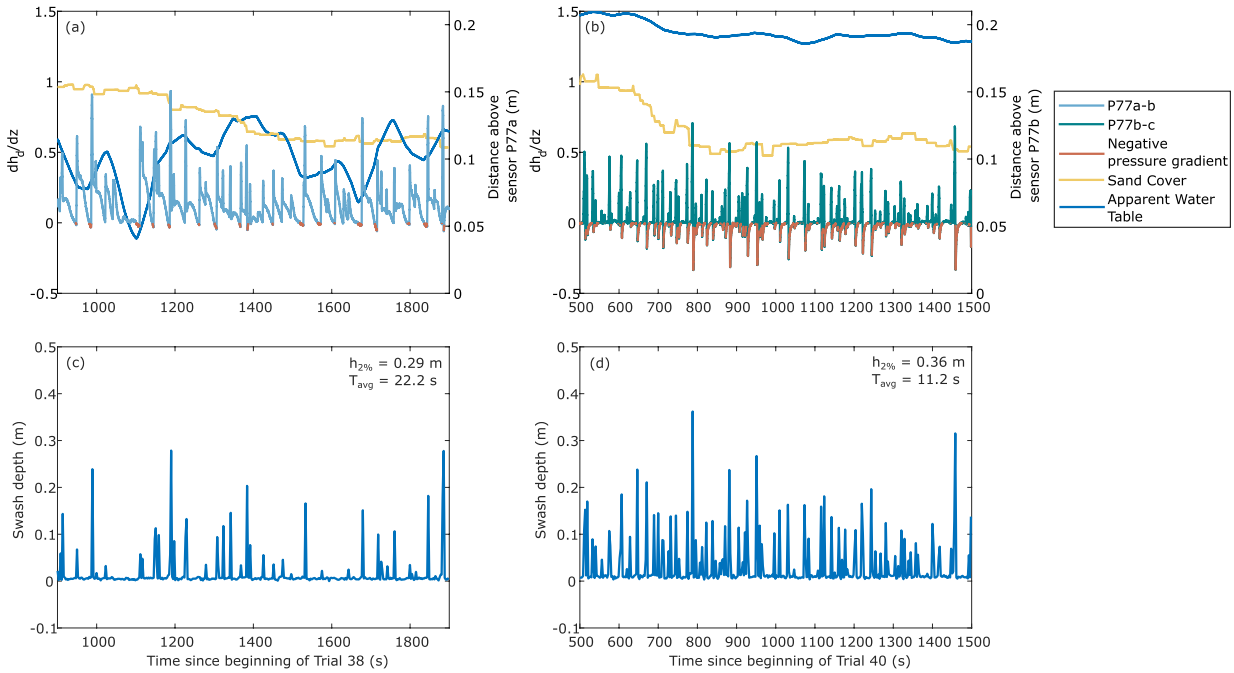

Figure 7. A comparison of upward-directed pressure gradients at the same distance below the sand surface at two different points in time (Trial 38 and 40). (a) dh_e/dz between pressure sensors P77a (upper) and P77b (lower) in brown, as the sand surface cover above sensor P77a (blue) eroded from 0.16 to 0.11 m during Trial 38. (b) dh_e/dz between pressure sensors P77b (upper) and P77c (lower) in brown, as the sand surface cover above sensor P77b (blue) eroded from 0.16 to 0.11 m during Trial 40. (c) Swash events recorded at the sensor location ($x = 77$ m) during Trial 38 (a). (d) Swash events recorded at the sensor location ($x = 77$ m) during Trial 40.

As the sand cover above sensor P77a eroded from 0.16 to 0.1 m, there were a few instances in which the dynamic pressure gradient between sensors P77a and P77b was negative. Those instances occurred just before a spike in positive dynamic pressure gradient due to the next uprush (Figure 7). The average depth of the greatest two percent of swash events ($h_{2\%}$) was 0.29 m (Figure 7c), and the average swash return period (T_{avg}) was 22.2 s.

As the sand cover above sensor P77b eroded from 0.16 to 0.1 m, there were more instances of negative dynamic pressure gradients. Dynamic pressure gradients as negative as −0.35 were recorded. Instances of negative pressure gradients occurred during backwash, similar to the example given in Figure 6. $h_{2\%}$ of the swash was 0.36 m, nearly 10 cm greater than when the same sand cover was above sensor P77a during Trial 38. T_{avg} in this period was 11.2 s, approximately half of the average swash return period when the same sand cover was over sensor P77a during Trial 38.

The moisture sensors co-located with the upper sensors (M77a co-located with P77a and M77b co-located with P77b) both had reached a steady state, where some undetermined amount of gas within the pore spaces is assumed to be present, prior to the time periods in Figure 7 (Figure 5). While the absolute water content at the times and locations pictured may have been different between sensors, both sensors had reached steady partial saturation before the events shown in Figure 7.

3.4. Momentary Liquefaction

To examine the potential occurrence of momentary liquefaction events, thresholds specified by Turner and Nielsen (1997), Mory et al. (2007), Michallet et al. (2009), and Sumer and Fredsøe (2002) were used. The thresholds for momentary liquefaction are shown for pressure sensors measurements during Trial 39, beginning after a spinup period to allow the groundwater to stabilize at the beginning of the trial (Figure 8). Trial 39 is the last trial in which all pressure sensors at $x = 77$ m remained in the sand. The sand cover above sensor P77a ranged from 0.07 to 0.09 m, and the sand cover above sensor P77b ranged from 0.17 to 0.19 m.

The liquefaction threshold suggested by Turner and Nielsen (1997) (Equation 1) is based on the concept of critical fluid velocity driven by a pressure gradient according to Darcy's law (Holtz & Kovacs, 1981). The hydraulic conductivity for this calculation was based on the Hazen equation $\left(K = 0.01 D_{10}^2\right)$, using a D_{10} of 0.17 mm

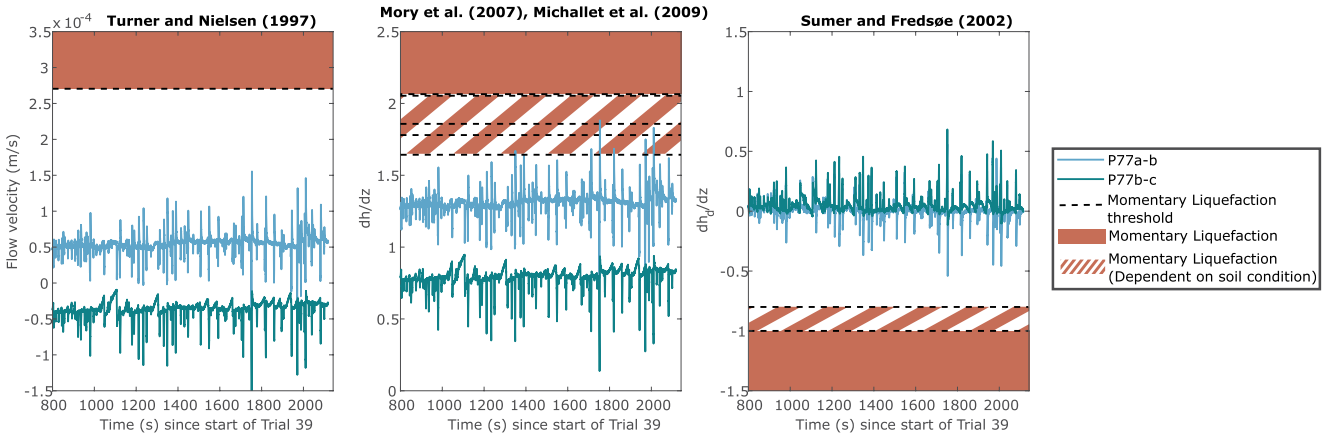

Figure 8. (a) Calculated flow velocities, (b) pressure gradients converted to meters, and (c) the dynamic pressure gradient converted to meters based on data collected by sensors P77a and P77b (light blue) and sensors P77b and P77c (blue-green). All panels display the same period of time from Trial 39. The shaded red areas indicate where liquefaction is expected to occur based on the threshold given in the subplot title. Red stripes indicate the range in which liquefaction is dependent on sediment conditions as described in the main text. Throughout the pictured time in Trial 39, the sand cover above sensor P77a eroded from 0.09 to 0.07 m, and the sand cover above sensor P77b eroded from 0.19 to 0.17 m.

(Hazen, 1911). According to the Turner and Nielsen threshold, no momentary liquefaction events were recorded between sensors P77a-b or P77b-c during the shown time period (Figure 8).

A range of liquefaction thresholds were also calculated based on Mory et al. (2007) and Michallet et al. (2009) (Equation 2), which account for gas content within the sediment. Mory et al. (2007) and Michallet et al. (2009) both give a low estimate of the liquefaction threshold for loose sediment conditions and high gas content ($\rho_s = 2{,}600$, $\epsilon = 0.5$, $C_{gas} = 0.06$) and a high estimate of the liquefaction threshold for compact sediment conditions and low gas content ($\rho_s = 2{,}750$, $\epsilon = 0.4$, $C_{gas} = 0.01$). A theoretical minimum for the liquefaction threshold was also calculated using the loose sediment conditions with $C_{gas} = 0.30$ based on measurements of void ratio and saturation in the intertidal zone (Florence et al., 2022). During the period of observation in Figure 8, six events exceed the theoretical minimum threshold, and two events reach the range in which momentary liquefaction may occur depending on soil conditions as described above. No events reach the threshold at which liquefaction is likely regardless of soil conditions.

Another threshold of liquefaction was calculated based on the definition of momentary liquefaction (Sumer & Fredsøe, 2002) (Equation 3). Here, only the dynamic pressure was considered (Equation 4). To remain consistent with the sign convention used for this calculation throughout the paper, the sign convention in Figure 8c is opposite to the sign convention of Figures 8a and 8b. For typical void ratios of sands, γ_{sat} ranges between 18 and 20 kN/m^3 (Budhu, 2010). Based on this range, the expression for the critical negative dynamic pore pressure gradient required to trigger momentary liquefaction became $dh_d/dz \approx -0.83$ to -1. No events between either sensor pair reach this threshold for liquefaction during the presented time interval.

4. Discussion

The swash zone is a highly dynamic region, and there is not currently a complete understanding of the processes controlling scarp formation. Results (Figures 6 and 7) showed the increasing occurrence of upward-directed pressure gradients in the sand at the base of the developing scarp, which can increase the potential for erosion and scour (Butt et al., 2001; Tonkin et al., 2003). However, momentary liquefaction based on the thresholds developed by Turner and Nielsen (1997), Mory et al. (2007), Michallet et al. (2009), and Sumer and Fredsøe (2002) was rarely observed. Therefore, in this section, the implications of upward-directed pressure gradients and momentary liquefaction in the swash zone are discussed. Afterward, a simple framework for scarp formation and development is proposed to contextualize destabilization caused by upward-directed pressure gradients with other processes occurring during scarp formation.

4.1. Sediment Destabilization and Momentary Liquefaction

Throughout the experiment, an increase in the frequency and magnitude of upward-directed dynamic pressure gradients was observed. Upward-directed dynamic pressure gradients exert a force upward on the sand and

decrease the effective weight, which can potentially destabilize the sand and promote erosion. Given two time periods with the same sand cover and with sediments under the apparent water table, instances of destabilizing pressure gradients increased with decreasing swash return period and increasing swash depth. Therefore, swash frequency and depth are important factors in determining whether destabilizing pressure gradients occur.

While evidence of destabilizing pressure gradients was observed, there were nearly no observations of momentary liquefaction based on the available criteria (Michallet et al., 2009; Mory et al., 2007; Sumer & Fredsøe, 2002; Turner & Nielsen, 1997). However, the thresholds used did not fully capture the situation observed in this study. The Turner and Nielsen (1997) threshold is limited by the need to assume a hydraulic conductivity in the absence of direct measurements. The method also does not account for gas content within the sand. The Mory et al. (2007) and Michallet et al. (2009) equations do account for gas content, however, accurately measuring the gas content of sand is difficult and was not undertaken for this experiment. Additionally, the equations and associated gas content measurements were developed for submerged sediment, and were not designed for use in the swash zone. While the accuracy of the equations for estimating a liquefaction threshold have been confirmed in the lab (Stark et al., 2022), sediment compaction and, possibly more importantly, the gas content, has the potential to change dramatically on a wave by wave basis in the swash zone. A theoretical minimum threshold for liquefaction was estimated using the Mory et al. (2007) and the Michallet et al. (2009) equations and using a theoretical upper limit for gas content in the swash zone. However, as Equation 2 is empirical and was not developed in the swash zone, the calculation of these thresholds should be used as a first order estimate until the dynamics of gas content within the swash zone are better understood. By simply using the dynamic pressure (i.e., with static pressure filtered out) to calculate momentary liquefaction (Equation 3), impacts to the pressure gradient from fluid flow within the sand may be unaccounted for.

Based on the thresholds of Turner and Nielsen (1997), Mory et al. (2007), Michallet et al. (2009), and Sumer and Fredsøe (2002), momentary liquefaction did not occur significantly enough to be considered a major driver of erosion. However, the reduction of effective weight caused by upward-directed pressure gradients occurred often in the upper part of the sand as wave conditions became more energetic and the apparent groundwater table rose in elevation (Figures 7 and 8). Thus, the destabilizing pressure gradients may be a driver of the erosion occurring seaward of the slope discontinuity during scarp formation.

4.2. Scarp Formation

While destabilizing pressure gradients may have been impacting the development of the scarp, we argue that destabilizing gradients alone are not enough to cause the formation of a scarp. We propose a simple model for the formation of a scarp during erosive conditions: a scarp begins as a discontinuity in slope due to process or structural controls, and the discontinuity steepens and progresses landward as a result of erosion seaward of the scarp. As the beachface seaward of the slope discontinuity continues eroding, the steepening slope of the discontinuity causes sediments to be eroded more easily. Steepening and landward progression of the slope discontinuity continues until a vertical scarp has formed (Figure 9).

During erosion of the dune tested in this experiment, the initial discontinuity developed due to wave-driven accretion that occurred on the upper beachface between the $R_{2\%}$ and $R_{\max}$ exceedance limits (Trials 28–36, $x = 75$–77). Erosion seaward of the discontinuity began occurring soon thereafter (Trial 34, $x = 76$ m), and is considered the beginning of scarp development. The discontinuity formed at approximately the $R_{2\%}$ runup extent and progressed landward at the same rate as the $R_{2\%}$ runup extent throughout the period of scarp formation (Figure 4).

Seaward of the developing scarp, the dune hydrodynamics provided the conditions for erosion to take place. The groundwater reached a steady, partially saturated state (Trial 34, $x = 77$ m, Figure 5), allowing pressure waves to propagate through the sand and create conditions for destabilization within the surface sediments. Sand destabilization increased with swash depth (Figure 8), and decreased with distance into the sand and the swash return period (Figure 7). The destabilization events may have contributed to the increasing erosion volumes observed seaward of the developing scarp (Trials 34–40, $x = 77$–78 m).

Erosion events driven by destabilizing pressure gradients may not be solely responsible for scarp formation; however, future work on other drivers of scarp formation can still fit into the conceptual model of scarp formation. Swash zone sediment transport is a dynamic and ongoing field of research, and the observations presented in this study highlight one specific swash zone erosion process—destabilization caused by pressure gradients. It

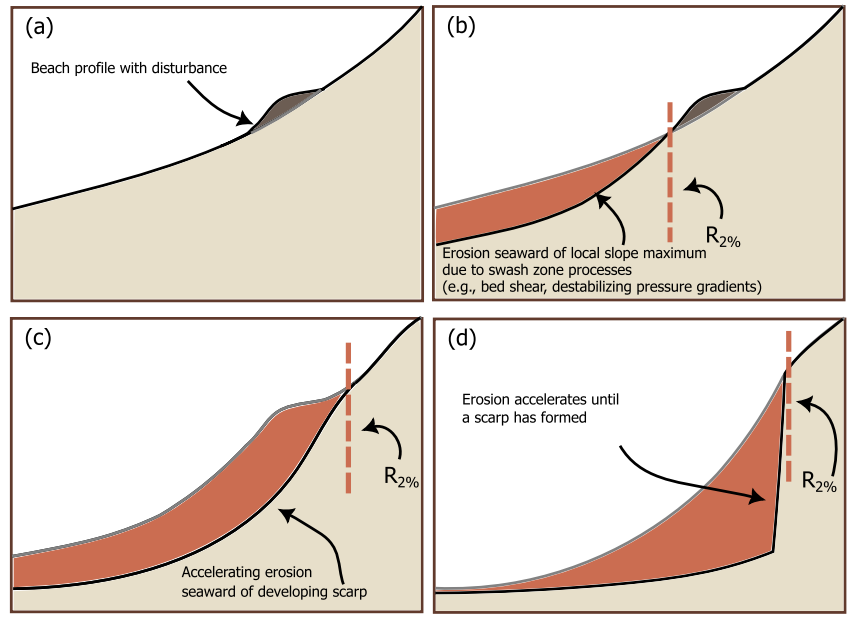

Figure 9. Schematic of a conceptual model for scarp formation. (a) A relatively smooth beach profile has a disturbance in the beach slope. (b) Erosion seaward of the discontinuity due to swash zone processes. In this study, these may have included destabilizing pressure gradients. (c) The steepening slope creates positive feedback and makes erosion of sediments easier, causing the scarp to steepen, grow, and progress landward. (d) Erosion accelerates until a vertical scarp face has formed.

is important to note that scarp formation during erosive conditions can be influenced by various other processes within the swash zone. Other processes that contribute to erosion seaward of the scarp could include feedbacks between the developing scarp and swash dynamics, dynamics in bedload and suspended load transport, and boundary layer dynamics. Physical mechanisms for accretion were not directly tested in this study, but further work could identify if, for example, the accretion mechanism described in Baldock et al. (2001) is influencing the development of scarps.

Destabilizing pressure gradients were identified to be related to scarp formation in this study and were observed to increase in magnitude as erosion rates increased. However, more work is needed to fully understand the effect of pressure gradients on erosion in the swash zone. A greater density of shallowly buried pressure sensors would aid in understanding the temporal and spatial evolution of destabilizing pressure gradients, and a better understanding of the gas content within swash zone sediments would help to identify whether or not liquefaction is actually occurring. More work is also needed to better understand the impacts of groundwater on scarp formation. We recommend that future work includes the development of a modified Shields parameter, such as those developed by Turner and Masselink (1998) and Yeh and Mason (2014), to include both the effect of destabilizing pressure gradients and the increasing slope of the developing scarp during erosive conditions.

5. Conclusion

A beach dune was tested under increasing wave heights and water levels in a large scale lab experiment to identify the physical mechanisms of scarp formation. After approximately 14 hr of waves (Trial 34), a slope discontinuity formed and grew steeper and taller as it moved landward. After approximately 18 hr of waves (Trial 41), the slope discontinuity had turned into a vertical scarp that continued retreating over the remainder of the experiment through slumping. The initial slope discontinuity developed due to accretion between the $R_{2\%}$ exceedance extent and the $R_{\max}$ exceedance extent. The dune scarp formed and progressed landward at approximately the $R_2\%$ exceedance extent of runup due to erosion between the $R_{2\%}$ and $R_{10\%}$ exceedance extents as waves and water levels increased. After the scarp began progressing landward, there was no longer significant wave-driven accretion.

The patterns of erosion and accretion that contributed to the formation of the scarp were influenced by the dune subsurface hydrodynamics. During the formation of the scarp, the apparent water table was elevated above the

SWL due to wave infiltration. In the area seaward of the maximum runup, the sand reached a steady state of partial saturation where the volumetric water content remained constant, but full saturation was unlikely due to gas bubbles expected to be in the sand. In these steady, partially saturated conditions, destabilizing upward-directed pressure gradients within the sand occurred during backwash. These destabilizing events increased in frequency as swash depth and frequency increased, and decreased with depth into the sand. Apart from six swash events that may have caused liquefaction dependent on the sediment characteristics, the destabilizing events observed did not exceed several theoretical thresholds for momentary liquefaction tested in this study (Michallet et al., 2009; Mory et al., 2007; Sumer & Fredsøe, 2002; Turner & Nielsen, 1997).

We propose a conceptual model of scarp formation in which a scarp begins with a discontinuity either caused by process controls (e.g., changes in water level or wave conditions) or structural controls (e.g., tire tracks on the beach or a dune toe). After the discontinuity forms, erosion seaward of the discontinuity causes the growth, steepening, and landward progression of a scarp. In this experiment, wave-driven accretion contributed to the formation of the initial discontinuity, and destabilizing pressure gradients contributed to the erosion seaward of the scarp. Future work on erosion and accretion in the swash zone during extreme events can use this conceptual model to explore other processes that drive the formation of beach and dune scarps.

Data Availability Statement

Experimental data, sensor configurations, and forcing conditions are available on the NSF NHERI data depot at https://doi.org/10.17603/ds2-nf3k-fe18 (Bond & Wengrove, 2023).

Acknowledgments
This material is based upon work supported by the National Science Foundation under Grants 1519679, 1756714, 1756477, and 1756449. J. Puleo was additionally funded under USACE/USCRP W912HZ-19-2-0041 and USACE/USCRP W912HZ-18-P-0124. T.M. Evans was funded under CMMI-1933355. We also thank Pedro Lomónaco and Tim Maddux for their help in the wave lab. This work would not have been possible without the help of Benjamin Tsai, Yashar Rafati, Rachel Innocenti, Seok-Bong Lee, Jordan Converse, Marivi Moragues Gomez, Jeremy Smith, Sydney Cargill, Ihan-Jarek Acevedo, Rob Lewis, and Nessa Garrey during the experiment. We would also like to thank the anonymous reviewers whose thoughtful reviews of the manuscript have made it much more clear and impactful.

References

Bakhtyar, R., Brovelli, A., Barry, D. A., & Li, L. (2011). Wave-induced water table fluctuations, sediment transport and beach profile change: Modeling and comparison with large-scale laboratory experiments. *Coastal Engineering*, *58*(1), 103–118. https://doi.org/10.1016/j.coastaleng.2010.08.004

Baldock, T. E., Baird, A. J., Horn, D. P., & Mason, T. (2001). Measurements and modeling of swash-induced pressure gradients in the surface layers of a sand beach. *Journal of Geophysical Research*, *106*(C2), 2653–2666. https://doi.org/10.1029/1999jc000170

Bond, H., & Wengrove, M. (2023). *Dune subsurface hydrodynamics during an extreme event*. Designsafe-CI. https://doi.org/10.17603/DS2-NF3K-FE18

Bonte, Y., & Levoy, F. (2015). Field experiments of beach scarp erosion during oblique wave, stormy conditions (Normandy, France). *Geomorphology*, *236*, 132–147. https://doi.org/10.1016/j.geomorph.2015.02.014

Budhu, M. (2010). *Soil mechanics and foundations* (3rd ed.). John Wiley & Sons, Inc.

Bujan, N., Cox, R., & Masselink, G. (2019). From fine sand to boulders: Examining the relationship between beach-face slope and sediment size. *Marine Geology*, *417*(June), 106012. https://doi.org/10.1016/j.margeo.2019.106012

Butt, T., Russell, P., & Turner, I. L. (2001). The influence of swash infiltration—Exfiltration on beach face sediment transport: Onshore or offshore? *Coastal Engineering*, *42*(1), 35–52. https://doi.org/10.2208/prohe.47.1327

Conley, D. C., & Inman, D. L. (1994). Vented oscillatory boundary layers. *Journal of Fluid Mechanics*, *273*, 261–284. https://doi.org/10.1017/S002211209400193X

Davidson, S. G., Hesp, P. A., & Silva, G. M. D. (2020). Controls on dune scarping. *Progress in Physical Geography*, *44*(6), 923–947. https://doi.org/10.1177/0309133320932880

Duncan, J. R., Jr. (1964). The effects of water table and tide cycle on swash-backwash sediment distribution and beach profile development. *Marine Geology*, *2*(3), 186–197. https://doi.org/10.1016/0025-3227(64)90039-8

Eliot, I. G., & Clarke, D. J. (1988). Semi-diurnal variation in beachface aggradation and degradation. *Marine Geology*, *79*(1–2), 1–22. https://doi.org/10.1016/0025-3227(88)90153-3

Emery, K., & Foster, J. (1948). Water tables in marine Beaches. *Journal of Marine Research*, *7*(3), 644–654. Retrieved from https://elischolar.library.yale.edu/journal_of_marine_research/693/

Erikson, L. H., Larson, M., & Hanson, H. (2007). Laboratory investigation of beach scarp and dune recession due to notching and subsequent failure. *Marine Geology*, *245*(1–4), 1–19. https://doi.org/10.1016/j.margeo.2007.04.006

Feagin, R., Innocenti, R., Bond, H., Wengrove, M., Huff, T., Tsai, B., et al. (2023). Does vegetation accelerate coastal dune erosion during extreme events? *Science Advances*, *9*(24), eadg7135. https://doi.org/10.1126/sciadv.adg7135

Florence, M., Stark, N., Raubenheimer, B., & Elgar, S. (2022). Nearshore vertical pore pressure gradients and onshore sediment transport under tropical storm forcing. *Journal of Waterway, Port, Coastal, and Ocean Engineering*, *148*(6), 1–7. https://doi.org/10.1061/(asce)ww.1943-5460.0000723

Gourlay, M. (1992). Wave set-up, wave run-up and beach water table: Interaction between surf zone hydraulics and groundwater hydraulics. *Coastal Engineering*, *17*(1–2), 93–144. https://doi.org/10.1016/0378-3839(92)90015-M

Gratiot, N., & Mory, M. (2000). Wave-induced sea bed liquefaction with application to mine burial (Vol. 2). Retrieved from https://onepetro.org/ISOPEIOPEC/proceedings-abstract/ISOPE00/All-ISOPE00/ISOPE-I-00-201/6959

Guisado-Pintado, E., & Jackson, D. W. (2019). Coastal impact from high-energy events and the importance of concurrent forcing parameters: The cases of storm Ophelia (2017) and storm Hector (2018) in NW Ireland. *Frontiers in Earth Science*, *7*(August), 1–18. https://doi.org/10.3389/feart.2019.00190

Hazen, A. (1911). Discussion of 'Dams on sand foundations' by A.C. Koenig. *Transactions of the American Society of Civil Engineers*, *73*, 199–203.
Heiss, J. W., Puleo, J. A., Ullman, W. J., & Michael, H. A. (2015). Coupled surface-subsurface hydrologic measurements reveal infiltration, recharge, and discharge dynamics across the swash zone of a sandy beach. *Water Resources Research*, *51*(11), 8834–8853. https://doi.org/10.1002/2015WR017200.A
Holman, R. (1986). Extreme value statistics for wave run-up on a natural beach. *Coastal Engineering*, *9*(6), 527–544. https://doi.org/10.1016/0378-3839(86)90002-5
Holtz, R. D., & Kovacs, W. D. (1981). *An introduction to geotechnical engineering*. Prentice Hall.
Hoque, M. A., & Asano, T. (2007). Numerical study on wave-induced filtration flow across the beach face and its effects on swash zone sediment transport. *Ocean Engineering*, *34*(14–15), 2033–2044. https://doi.org/10.1016/j.oceaneng.2007.02.004
Leatherman, S. P. (1979). Beach and dune interactions during storm conditions. *Journal of Engineering Geology*, *12*(4), 281–290. https://doi.org/10.1144/gsl.qjeg.1979.012.04.05
Michallet, H., Mory, M., & Piedra-Cueva, I. (2009). Wave-induced pore pressure measurements near a coastal structure. *Journal of Geophysical Research*, *114*(6), 1–18. https://doi.org/10.1029/2008JC005071
Mory, M., Michallet, H., Bonjean, D., Piedra-Cueva, I., Barnoud, J. M., Foray, P., et al. (2007). A field study of momentary liquefaction caused by waves around a coastal structure. *Journal of Waterway, Port, Coastal, and Ocean Engineering*, *133*(1), 28–38. https://doi.org/10.1061/(ASCE)0733-950X(2007)133:1(28)
Nielsen, P. (1992). *Coastal bottom boundary layers and sediment transport*. World Scientific Publishing Co. Pte. Ltd.
Nielsen, P., Robert, S., Møller-Christiansen, B., & Oliva, P. (2001). Infiltration effects on sediment mobility under waves. *Coastal Engineering*, *42*(2), 105–114. https://doi.org/10.1016/S0378-3839(00)00051-X
Nishi, R., Sato, M., & Wang, H. (1995). Field observation and numerical simulation of beach and dune scarps. *Proceedings of the Coastal Engineering Conference*, *3*, 2434–2448. https://doi.org/10.1061/9780784400890.177
NOAA. (2023). Tides and currents: 8534720 Atlantic City, NJ.
O'Dea, A., Brodie, K. L., & Hartzell, P. (2019). Continuous coastal monitoring with an automated terrestrial lidar scanner. *Journal of Marine Science and Engineering*, *7*(2), 37. https://doi.org/10.3390/jmse7020037
Okusa, S. (1985). Wave-induced stresses in unsaturated submarine sediments. *Géotechnique*, *35*(4), 517–532. https://doi.org/10.1680/geot.1985.35.4.517
Paldor, A., Stark, N., Florence, M., Raubenheimer, B., Elgar, S., Housego, R., et al. (2022). Coastal topography and hydrogeology control critical groundwater gradients and potential beach surface instability during storm surges. *Hydrology and Earth System Sciences*, *26*(23), 5987–6002. https://doi.org/10.5194/hess-26-5987-2022
Palmsten, M. L., & Holman, R. A. (2011). Infiltration and instability in dune erosion. *Journal of Geophysical Research*, *116*(C10), C10030. https://doi.org/10.1029/2011JC007083
Palmsten, M. L., & Holman, R. A. (2012). Laboratory investigation of dune erosion using stereo video. *Coastal Engineering*, *60*, 123–135. https://doi.org/10.1016/J.COASTALENG.2011.09.003
Pontiki, M., Puleo, J., Bond, H., Wengrove, M., Feagin, R., Hsu, T.-J., & Huff, T. (2023). Geomorphic response of a coastal Berm to storm surge and the importance of sheet flow dynamics. *Journal of Geophysical Research: Earth Surface*, *128*(10), e2022JF006948. https://doi.org/10.1029/2022JF006948
Pujara, N., Liu, P. L., & Yeh, H. H. (2015). An experimental study of the interaction of two successive solitary waves in the swash: A strongly interacting case and a weakly interacting case. *Coastal Engineering*, *105*, 66–74. https://doi.org/10.1016/j.coastaleng.2015.07.011
Raubenheimer, B., Guza, R. T., & Elgar, S. (1999). Tidal water table fluctuations in a sandy ocean beach. *Water Resources Research*, *35*(8), 2313–2320. https://doi.org/10.1029/1999WR900105
Roelvink, J., Reniers, A., Van Dongeren, A., van Thiel de Vries, J., Lescinski, J., & McCall, R. (2010). *XBeach model description and manual*. Unesco-IHE Institute for Water Education. Retrieved from https://svn.oss.deltares.nl/repos/openearthtools/sandbox/DSD_2014/XBeachExecutable/xbeach_manual.pdf
Sakai, T., Hatanaka, K., & Mase, H. (1992). Wave-induced effective stress in seabed and its momentary liquefaction. *Ocean Engineering*, *118*(2), 202–206. https://doi.org/10.1061/(ASCE)0733-950X(1992)118:2(202)
Sallenger, A. H. (2000). Storm impact scale for barrier islands. *Journal of Coastal Research*, *16*(3), 890–895. Retrieved from https://www.jstor.org/stable/4300099
Sargent, F. E., & Birkemeier, W. A. (1985). *Application of the Dutch method for estimating storm-induced dune erosion (technical report)*. Coastal Engineering Research Center. Retrieved from https://hdl.handle.net/11681/20406
Seymour, R., Guza, R. T., O'Reilly, W., & Elgar, S. (2005). Rapid erosion of a small southern California beach fill. *Coastal Engineering*, *52*(2), 151–158. https://doi.org/10.1016/j.coastaleng.2004.10.003
Sherman, D., & Nordstrom, K. (1985). Beach scarps. *Annals of Geomorphology*, *29*(2), 139–152. https://doi.org/10.1127/zfg/29/1985/139
Stark, N., Mewis, P., Reeve, B., Florence, M., Piller, J., & Simon, J. (2022). Vertical pore pressure variations and geotechnical sediment properties at a sandy beach. *Coastal Engineering*, *172*(June 2021), 104058. https://doi.org/10.1016/j.coastaleng.2021.104058
Sumer, B. M., & Fredsøe, J. (2002). The mechanics of scour in the marine environment.
Terzaghi, K. (1943). *Theoretical soil mechanics*. J. Wiley and Sons, Inc.
Thornton, E. B., MacMahan, J., & Sallenger, A. H. (2007). Rip currents, mega-cusps, and eroding dunes. *Marine Geology*, *240*(1–4), 151–167. https://doi.org/10.1016/j.margeo.2007.02.018
Tonkin, S., Yeh, H., Kato, F., & Sato, S. (2003). Tsunami scour around a cylinder. *Journal of Fluid Mechanics*, *496*, 165–192. https://doi.org/10.1017/S0022112003006402
Turner, I. L., & Masselink, G. (1998). Swash infiltration-exfiltration and sediment transport. *Journal of Geophysical Research*, *103*(C13), 30813–30824. https://doi.org/10.1029/98JC02606
Turner, I. L., & Nielsen, P. (1997). Rapid water table fluctuations within the beach face: Implications for swash zone sediment mobility? *Coastal Engineering*, *32*(1), 45–59. https://doi.org/10.1016/s0378-3839(97)00015-x
van Bemmelen, C. W., de Schipper, M. A., Darnall, J., & Aarninkhof, S. G. (2020). Beach scarp dynamics at nourished beaches. *Coastal Engineering*, *160*, 103725. https://doi.org/10.1016/j.coastaleng.2020.103725
van de Graaff, J. (1994). Coastal and dune erosion under extreme conditions. *Journal of Coastal Research Special Issue*, *12*(12), 253–262. Retrieved from http://www.jstor.org/stable/25735602

Van Rijn, L. C., Tonnon, P. K., Sánchez-Arcilla, A., Cáceres, I., & Grüne, J. (2011). Scaling laws for beach and dune erosion processes. *Coastal Engineering*, *58*(7), 623–636. https://doi.org/10.1016/j.coastaleng.2011.01.008

WW3DG. (2019). User manual and system documentation of WAVEWATCH III version 6.07, the WAVEWATCH III development group. Technical note 326 pp. + Appendices, NOAA/NWS/NCEP/MMAB.

Yeh, H., & Mason, H. B. (2014). Sediment response to tsunami loading: Mechanisms and estimates. *Géotechnique*, *64*(2), 131–143. https://doi.org/10.1680/geot.13.P.033